

Treatment of contact separation in Eulerian high speed multimaterial dynamic simulations

N. K. Rai^a, A. Kapahi^a and H. S. Udaykumar^{a*}

^a*Department of Mechanical and Industrial Engineering, The University of Iowa, Iowa City, IA-52242, USA*

**Corresponding author email: ush@engineering.uiowa.edu*

1. ABSTRACT

A frictionless contact separation treatment in a sharp-interface Eulerian framework is presented to handle the general situation of high speed impact and separation of materials. The algorithm has been developed for an established Eulerian based Cartesian grid multimaterial flow code in which the interfaces are tracked in a sharp manner using a standard narrow-band levelset approach. Boundary conditions have been applied using a modified ghost fluid method for elasto-plastic materials. The sharp interface treatment maintains the distinct interacting interfaces without smearing the contact zone while also removing the difficulties associated with Lagrangian moving mesh entities in contact-separation situations. The algorithm has been tested and verified against experimental and numerical results for three different problems in the high strain rate regime which involve contact, separation and sliding of materials.

Keywords: Eulerian; Sharp Interface Methods; Cartesian Grid Methods; Level Set Methods; Ghost Fluid Method (GFM); High Velocity Impact; Frictionless Contact, Separation, Flyer plate Impact.

2. INTRODUCTION

High speed impact leading to large deformation, penetration and fragmentation arises in many applications including munition-target interaction[1, 2], geological impact dynamics[3, 4], shock-processing of powders[5, 6] etc. In these situations large deformations of materials are produced due to the propagation of nonlinear elasto-plastic shock waves generated due to the impact. Numerical simulation of impact problems involving multimaterial interactions demands accurate implementation of interfacial conditions at the region of impact. In Eulerian multimaterial impact formulations[7] material interface treatments assume an artificial bonding between the impacting interfaces of the adjacent materials because of the presence of a continuous normal velocity field at material interfaces. Due to this, problems in which impact, separation and sliding of materials play an important role in the dynamics are not well handled in Eulerian methods. On the other hand, Lagrangian methods handle contact and separation rather naturally because of: a)

explicit tracking of interfaces, b) the presence of independent velocity fields in the interacting materials and c) the kinematic contact constraints which couple the independent fields at the impacting surface. However, in Lagrangian techniques detecting contact between surfaces can pose challenges and maintaining “good” meshes in the course of large material deformations can be onerous. Because Eulerian methods operate on fixed meshes while the materials flow through the fixed (typically Cartesian) meshes, these aforementioned difficulties with Lagrangian techniques are mitigated. Therefore, an approach that combines the desirable features of Eulerian and Lagrangian methods for handling multimaterial interactions involving contact and separation would be highly useful. This paper describes such an approach in a sharp interface Eulerian framework[8] that avoids problems associated with Lagrangian mesh management while clearly delineating interacting material interfaces and applying local contact-separation conditions.

To handle the problem of large deformations, an Eulerian formulation is an appealing choice compared to a Lagrangian approach as problems related to mesh distortion and remeshing of the domain can be avoided in the Eulerian setting. However, both the formulations suffer from their own strengths and weaknesses in high strain rate problems. The relative advantages and disadvantages of both the formulations have been discussed by Anderson[9]. In the field of contact mechanics, much work has been done in the Lagrangian when compared to the Eulerian framework. In the regime of high speed impact, a two-dimensional finite contact algorithm developed by Taylor and Flanagan[10] for the PRONTO2D explicit dynamics code is a common starting point. This algorithm has the capability to handle impact and separation of materials for frictionless as well as frictional contact. The algorithm uses the master-slave approach to designate impacting bodies. It is a two-step method in which first a predictor step predicts the nodal positions, velocities and acceleration of the master body and then the corrector step calculates the force required to prevent the penetration of master body into the slave body. This model has been used in the regime of high strain rate problems as in the work of Camacho and Ortiz[11]. The Lagrangian contact algorithm by Benson and Hallquist[12] developed for DYNA2D (a nonlinear explicit finite element software) is also well known for its capabilities to handle mechanical interaction of two bodies or self contact in the same body. This contact algorithm has been used in the work of Batra and Stevens[13]. Also, Belytchko et. al. [14] proposed a new contact detection algorithm in the Lagrangian framework based on the moment method in meshfree discretization that can handle general contact situations.

In Eulerian multimaterial impact computations the treatment of contact, separation and sliding is not as well developed as in the Lagrangian case. One of the notable works by Benson[15, 16] to handle both frictionless and frictional contact in an Eulerian framework using a mixture theory approach shows the capability of handling impact and separation of materials. The mixture theory has been used to calculate the mean stress at the interface between the interacting materials. The nonlinear contact constraint equations have been solved to impose the constraints for friction, frictionless sliding and separation. Mixture theory based approaches hinge on the proper physical treatment of the materials residing in the mixed cells and on ascribing suitable continuum models for the mixed materials. Assumptions of local equilibrium in the mixed cells must be invoked, and the problems of coexisting materials of vastly different impedances inside one element must be

addressed. The work of Vitali and Benson [17-19] using extended finite element method (X-FEM) in arbitrary Eulerian Lagrangian (ALE) formulations overcomes problems associated with mixture theories in handling sliding and separation and shows the capability of handling friction and frictionless contact. In these works, the limitation of mixture theory vis-à-vis the prediction of spurious stresses in mixed material elements has been overcome by creating independent velocity fields for the impacting materials in an X-FEM framework which allows local enrichment in the mixed material elements. Frictional and frictionless sliding has been handled by obtaining independent velocity and acceleration fields in the individual interacting materials at the region of impact. Separation between the different materials has been handled by introducing void material between the impacting materials once the mean stress at the interface becomes tensile. Also, the work by Vitali et. al.[20] to impose interfacial contact conditions using extended Eulerian formulation (XEM) shows the capability of handling frictionless sliding with separation in Godunov formulations.

The approach taken in this work is different from that in Vitali and Benson in that the current formulation is purely Eulerian, i.e. no Lagrangian phase (as in ALE) is involved. The interfaces are tracked using levelsets [21, 22], which means that they can be maintained in a sharp fashion, i.e. this is effectively an interface tracking approach rather than an interface reconstruction based on volume fractions. No mixture of materials at any stage of material-material interactions is involved as the sharp interface approach maintains the materials as separate entities delineated by two individually tracked levelset functions. The use of level set distance function for the representation of interfaces also simplifies the collision detection algorithm since information on distances between potentially interacting boundaries is implicitly and always available from the level set fields. Boundary conditions on the sharply separated and interacting sub-grid interfaces are incorporated implicitly using a modified ghost fluid method (MGFM)[23-25]. Since boundary conditions at the interface are satisfied implicitly using ghost fluid method (GFM), there is no need to solve additional non-linear equations to impose the contact constraints. The use of GFM to handle boundary conditions helps to create independent velocity fields in each material and frictionless sliding can be handled by coupling these fields at the interacting interfaces. In this framework, much like in the explicitly tracked Lagrangian contact formulations, separation between the materials occurs as a natural process of deformation [26-30], i.e. separation is not enforced by introducing a void phase in a mixed material but occurs simply as the consequence of evolving the sharp interfaces. This algorithm is purely local in implementation and can be used in a parallel computing framework[31] and can be easily extended to three dimensions.

In previous works [8, 26, 27] simulation of multi-material impact problems involving collision between the materials followed by large deformation, penetration and fragmentation were performed. However the contact treatment was rudimentary in that once materials impacted they remained in contact in the course of further interaction. This enforced prolonged contact of the materials leads to physically unrealistic results in certain type of problems where separation between the materials plays an important role. For example, in a flyer plate impact simulation separation between the plates plays an important role in the wave physics[32]. Also, in the ricochet of a projectile from a target separation and sliding of the projectile plays a crucial role in the

dynamics of both the projectile and the target [33]. Hence, to model these situations accurately appropriate boundary conditions need to be applied along with the contact conditions at the interacting interfaces. The contact model has been tested on three different types of multimaterial impact problems which involves impact and separation of materials at high strain rate. The three problems are:

- (a) Simulation of flyer plate experiment which involves impact of two deformable bodies.
- (b) Simulation of the Taylor bar impact test, which involves the situation when a deformable body impacts a rigid body.
- (c) Simulation of oblique impact of a projectile resulting in the ricochet of the impactor.

3. GOVERNING EQUATIONS

The governing equations and the description of the computational framework used in the current framework have been discussed in detail in previous work[26]. A brief description of the computing methodology is presented here for the sake of completeness.

The governing equations in Eulerian framework comprise a set of hyperbolic conservation laws[34, 35]. In Cartesian coordinates, the governing equations of conservation of mass, momentum and energy take the following form:

$$\frac{\partial \rho}{\partial t} + \text{div}(\rho \vec{V}) = 0 \quad (1)$$

$$\frac{\partial \rho \vec{V}}{\partial t} + \text{div}(\rho \vec{V} \otimes \vec{V} - \sigma) = 0 \quad (2)$$

$$\frac{\partial \rho E}{\partial t} + \text{div}(\rho E \vec{V} - \sigma \vec{V}) = 0 \quad (3)$$

$$\sigma = S - PI \quad (4)$$

$$\frac{\partial \rho S}{\partial t} + \text{div}(\rho \vec{V} S) + \frac{2}{3} \rho G \text{tr}(D)I - 2\rho GD = 0 \quad (5)$$

In equations (1-5) V is velocity, ρ is density, E is the specific internal energy, D is strain rate tensor, and G is the shear modulus of material. The stress state of material is specified by the Cauchy stress tensor σ (eqn. (4)) which consists of deviatoric part, S and dilatational part, P . The dilatational part, P (pressure) is given by the Mie-Gruneisen equation of state:

$$P(e, V) \approx \Gamma(V) \frac{(e - e_c(V))}{V} + P_c(V) = \Gamma \frac{e}{V} + f(V) \quad (6)$$

where, e_c and P_c denotes the reference internal energy and pressure at 0 K, and $\Gamma(V)$ is the Grüneisen parameter defined as

$$\Gamma(V) = V \left(\frac{\partial P}{\partial e} \right)_V = \frac{\Gamma_0 \rho_0}{\rho} \quad (7)$$

where, ρ_0 is the density of the unstressed material.

The function $f(V)$ is given as

$$f(V) = \begin{cases} \frac{\rho_0 c_0^2 \Phi}{(1 - s\Phi^2)^2} \left[1 - \frac{\Gamma}{2V} (V_0 - V) \right] & \text{if } V \leq V_0 \\ c_0^2 \left(\frac{1}{V} - \frac{1}{V_0} \right) & \text{if } V > V_0 \end{cases} \quad (8)$$

where, $\Phi = 1 - \frac{V}{V_0}$, $V = \frac{1}{\rho}$ and c_0 is the bulk sound speed. The material parameters for the equation of state are given in Table 2[36].

The materials in the current work have been modeled as elasto-plastic solids. Hence, the evolution of the deviatoric stress components is performed using the radial return algorithm[37] with the yield surface being estimated using the Johnson Cook strength model[38]. The Johnson Cook strength model is given by:

$$\sigma_Y = [A + B\varepsilon_p^n][1 + C \ln(\dot{\varepsilon}^*)][1 - T^{*m}] \quad (9)$$

where, σ_Y is the yield stress, ε_p is the equivalent plastic strain, $\dot{\varepsilon}^* = \dot{\varepsilon}/\dot{\varepsilon}_0$, $\dot{\varepsilon}$ is the plastic strain rate, and $\dot{\varepsilon}_0$ is the dimensionless plastic strain rate.

$$T^* = \frac{T_0 - T_{ref}}{T_{MELT} - T_{ref}}, T_0 \text{ is the temperature of the material, and}$$

$$T_{ref}, \text{ reference temperature} = 298 \text{ K and } \dot{\varepsilon}_0 = 1 \text{ s}^{-1}.$$

A, B, C, n, m, are model constants and their values for different materials have been specified in Table 1.

4. NUMERICAL TECHNIQUES

4.1 Numerical Scheme

The governing equations of mass, momentum, energy conservation along with the evolution equation of deviatoric stress components are solved using a 3rd order ENO (Essentially Non Oscillatory) scheme for the spatial discretization[39] and a 4th order Runge Kutta time

integration method in the current framework. The details regarding its implementation has been discussed in the previous work[8, 26].

4.2 Level Set Representation of Embedded Interface

In the current Eulerian framework the level set method[21, 22] has been used to represent embedded objects. The use of standard narrow band level set approach allows tracking the material interfaces in a sharp manner. The level set field, ϕ_l at any point is defined as the signed normal distance from the l^{th} immersed object with $\phi_l < 0$ inside the immersed boundary and $\phi_l > 0$ outside. The interface is implicitly determined by the zero level set field i.e. $\phi_l = 0$ contour represents the l^{th} immersed boundary (shown in figure 1).

The details regarding the implementation of the narrow band level set approach have been discussed in previous work[26]. Note that the level set field provides sharp delineation of all interacting interfaces so that even in those control volumes in which two or more interfaces coexist there is no mixing of the materials.

4.3 Ghost Fluid Treatment for Elasto-Plastic Material Interactions

Boundary conditions at the sharply defined material interfaces in multimaterial high velocity impact for the elasto-plastic solids have been enforced using a variant of the ghost fluid method(GFM) [23]. GFM relies on the definition of a band of ghost points corresponding to each phase of the interacting materials. The ghost points for a material are considered to be the points lying outside the material and real points are those which are inside. The band of ghost points are defined for each of the materials present in the computational domain. Once these ghost points are identified the next step is to populate the ghost field for each of the materials. The ghost field is obtained by constructing least-squares interpolation[40] of the field variables of real material points and imposing the appropriate interfacial conditions as discussed in section 4.4. This least - squares method has been found to work well in a wide range of situations of impact and penetration including situations that lead to the formation of small fragments.

Consider the example shown in figure 2 in which material 1 and material 2 are separated by an interface. The band of ghost points are identified separately for each of the material as shown in figure 2. Once the ghost points are identified, the ghost field for material 1 is constructed using the least square interpolation of the variables of the real points in material 1. Also, ghost field of material 2 is populated using the information of the real points of material 2. The application of least square field along with interfacial conditions leads to the population of ghost field for each materials.

Once the ghost points are identified and the values of the flow variables (e.g. density, velocities, pressure, temperature, stress components etc.) at these points are populated with the least square field, the two-material problem can be converted to two single-material problems consisting of real fields and their corresponding ghost fields. The use of GFM to convert a multimaterial problem into extended single material problems is advantageous for handling contact

situations as it provides independent fields for each material. These independent fields can easily be coupled based on the contact constraints locally at the impacting interface.

The detailed implementation of GFM framework using the least-squares approach is provided in previous work[26-28].

4.4 Applying Conditions at Interfaces

In the current Eulerian framework, the interaction of the materials with each other or with the surrounding void (in the case of free surfaces) is handled by the application of appropriate boundary conditions at the location of the sharp interfaces defined by the zero-level set contour. As the interfaces are arbitrarily aligned with the Cartesian grid, in order to apply the appropriate boundary conditions the stress tensor and velocity vector is transformed to the local normal and tangential directions. The normal and tangential velocity components are given as:

$$u_n = |\vec{u}_n| = \vec{u} \cdot \hat{n} \quad (10)$$

$$u_t = |\vec{u}_t| = \vec{u} \cdot \hat{t} \quad (11)$$

where, \vec{u} is the velocity vector, \hat{n} and \hat{t} are the local normal and tangential vectors and \vec{u}_n and \vec{u}_t are the normal and tangential velocity vectors.

The total stress tensor σ transformed in the local normal and tangential components is given as:

$$\tilde{\sigma} = J\sigma J^T = \begin{pmatrix} \tilde{\sigma}_{nn} & \tilde{\sigma}_{nt} \\ \tilde{\sigma}_{nt} & \tilde{\sigma}_{tt} \end{pmatrix} \quad (12)$$

where, the transformation matrix

$$J = \begin{pmatrix} n_x & n_y \\ t_x & t_y \end{pmatrix} \quad (13)$$

and $\tilde{\sigma}_{nn}$, $\tilde{\sigma}_{nt}$ are the normal stress components of the stress tensor and $\tilde{\sigma}_{tt}$ is the tangential component.

Three types of conditions apply at the interfaces in the test cases shown in this work:

4.4.1 Material-Material Conditions

In the case where materials interact with each other on parts of the interface, continuity of normal stress components and the continuity of normal velocity component are enforced. No constraint is applied on the tangential components of stress and velocity fields. The coupling of the normal component of stress and velocity and decoupling of the tangential components ensures frictionless sliding between the materials. Thus, at the interfaces:

$$[\bar{u} \cdot \hat{n}] = 0 \quad (14)$$

$$[\tilde{\sigma}_{nn}] = 0 \quad (15)$$

$$[\tilde{\sigma}_{nt}] = 0 \quad (16)$$

$$[P] = 0 \quad (17)$$

where, $\tilde{\sigma}_{nn}$ and $\tilde{\sigma}_{nt}$ are the normal components of the stress tensor, P is pressure.

4.4.2 Material-Void Conditions

This type of interfacial condition arises whenever the material interface interacts with a surrounding void, i.e. at a free surface. Conditions corresponding to physically consistent wave reflection phenomena are enforced at all free surfaces. Hence, zero-traction conditions on the normal stress components are enforced on those portions of the interface that are free surfaces, viz.:

$$\tilde{\sigma}_{nn} = 0 \quad (18)$$

$$\tilde{\sigma}_{nt} = 0 \quad (19)$$

4.4.3 Material-Rigid Solid Conditions

The rigid solid interface can also modeled in the current framework in situations when a deformable solid impacts on a rigid solid. The normal velocity at the colliding interface satisfies the following Dirichlet condition given as:

$$\bar{u} \cdot \hat{n} = U_n \quad (20)$$

where, U_n is the normal velocity of the rigid solid.

The continuity of the normal stress components is enforced and to ensure the free slip condition no constraint on the tangential stress components is applied.

4.5 Contact Algorithm

In order to handle collision or separation of materials at a common interface a frictionless contact algorithm is applied. The steps involved in the algorithm are explained sequentially below.

4.5.1 Detecting Collision

For all materials in the computational domain, the nodes in the Cartesian mesh that straddle the material interface are tagged as “interfacial nodes”; “interfacial nodes” are nodes that interact with the surrounding material. In the levelset framework these nodes are easily identified as those for which the levelset value for one of the neighbors is of the opposite sign. Thus these nodes represent the set of points in the domain that will be examined to determine if a collision is imminent or not. This procedure is carried out after each update of the interfaces. To detect

collision, for every interfacial node, the distance between itself (level set indexed l) and an adjoining level set (indexed k) is computed using the associated level set functions from:

$$\delta_{lk} = |\phi_l + \phi_k| \forall l \neq k \quad (21)$$

Note that not every level set evolved in the computational domain needs to be checked for collision. Collision checking is only conducted at an interfacial node if there are two level sets whose narrow bands overlap at that node. If the distance δ_{lk} computed between the two approaching level sets is less than a specified tolerance, then the node is marked as a “colliding node” (Figure 3). The tolerance value is set at $\kappa\Delta x$ where κ corresponds to the CFL number which depends on the (local) interface advection velocity used to evolve the level sets in time. Use of this preset tolerance preempts inter-penetration of level sets. Thus, at the instant at which an interfacial node is flagged for collision treatment to take effect the two colliding interfaces are separated by a distance $\kappa\Delta x$.

4.5.2 Kinematic and Stress Constraints

Use of the level set function facilitates the identification of colliding nodes between the materials. Once the colliding interfacial nodes are identified, the next step is to calculate the traction at the common interface between the neighboring materials, as shown in Figure 4(a). The tractions at the colliding nodes (e.g. $A1$ and $A2$ in figure 4(a)) are calculated using a least-squares approach[26] as explained in the next section.

4.5.3 Calculation of the stress field at the colliding nodes

The stress field in the region surrounding the colliding nodes is required to calculate the value of normal traction at the interface. The least-squares method to obtain the stress field is explained below:

Step 1: First, all the immediate neighbors (8 in 2D) of the interfacial point where the normal traction is to be calculated are identified. For example for point $A1$ the neighboring points are shown in figure 4(b).

Step 2: Once the neighbors are identified then the “real” material points are selected, i.e. points which lie inside the material; those points in the stencil that lie outside the material are rejected in the calculation of stress field as shown in figure 4(c). Once all the “real” neighboring points are identified the least-squares algorithm[40] is used to calculate the value of normal traction at the colliding nodes. First, the “real” neighboring material points are used to generate a bilinear interpolant given as:

$$T_n = a_1 + a_2x + a_3y + a_4xy \quad (22)$$

where, T_n is the bilinear interpolant to the normal traction field and a_i 's the unknown coefficients for the construction of the bilinear field.

The error in the approximation, e can be calculated from:

$$e = \sum_{i=1}^n (a_1 + a_2 x_i + a_3 y_i + a_4 x_i y_i - T_{n_i})^2 \quad (23)$$

where, n is the total number of available “real” neighboring material points and T_{n_i} is the computed value of normal traction at the neighboring nodes.

Least-squares minimization of the error (Eq. (23)) provides the coefficients of the interpolant (Eq. (20)) as follows:

$$\begin{bmatrix} \sum_{i=1}^n x_i^2 & \sum_{i=1}^n x_i y_i & \sum_{i=1}^n x_i^2 y_i & \sum_{i=1}^n x_i \\ \sum_{i=1}^n x_i y_i & \sum_{i=1}^n y_i^2 & \sum_{i=1}^n x_i y_i^2 & \sum_{i=1}^n y_i \\ \sum_{i=1}^n x_i^2 y_i & \sum_{i=1}^n x_i y_i^2 & \sum_{i=1}^n x_i^2 y_i^2 & \sum_{i=1}^n x_i y_i \\ \sum_{i=1}^n x_i & \sum_{i=1}^n y_i & \sum_{i=1}^n x_i y_i & \sum_{i=1}^n 1 \end{bmatrix} \begin{Bmatrix} a_1 \\ a_2 \\ a_3 \\ a_4 \end{Bmatrix} = \begin{Bmatrix} \sum_{i=1}^n T_{n_i} x_i \\ \sum_{i=1}^n T_{n_i} y_i \\ \sum_{i=1}^n T_{n_i} x_i y_i \\ \sum_{i=1}^n T_{n_i} \end{Bmatrix} \quad (24)$$

The value of the normal traction at the colliding node is then obtained from Eq. (22). If there are not enough neighboring points inside the materials to construct the least-squares field, then the field is not constructed and the value of traction at the colliding node itself is used. This eventuality only arises in the rare instances when there are small fragments or sharp re-entrant corners. For sufficiently well-resolved and smooth interfaces an adequate least-squares stencil is typically available.

Step 3: The normal traction obtained at the colliding nodes is next used to find the value of normal traction at the interface. First, considering any of the two materials shown in Figure 4(a), say material 1, the colliding nodes in this material are known a priori (labeled $A1$ in Figure 4(a)). Then the closest colliding node in material 2 with respect to material 1 is identified (labeled $A2$ in Figure 4(a)). These points $A1$ and $A2$ are used to find the normal traction value at the intermediate interfacial point (marked in Figure 4(a)) using Eq. (25).

$$T_n = \frac{w_2 T_{n_1} + w_1 T_{n_2}}{w_1 + w_2} \quad (25)$$

where, T_{n_1} and T_{n_2} are the normal tractions at the colliding points which form a pair across the interface and w_1 and w_2 are the weights given as:

$$w_1 = |\phi_1| \quad \text{and} \quad w_2 = |\phi_2| \quad (26)$$

where, ϕ_1 and ϕ_2 are the normal distance of the colliding nodes from the respective material interfaces (such as $A1$ from material 1 interface and $A2$ from material 2 interface).

The weights w_1 and w_2 gives measure of the influence of the respective colliding nodes on the interfacial point. So, the farther the colliding nodes is from the interface the lesser is its influence on the calculation of normal traction at the interfacial point.

The above process is applied to all the colliding nodes of material 1 in order to enforce the contact conditions at the interface along the parts of the interacting interfaces that qualify as colliding nodes.

4.4.4. Implementation of Contact Conditions:

Following contact and wave interactions at colliding interfaces, separation between the materials takes place when the materials pull apart from each other at the common impacting interface. The normal traction and normal velocity at the colliding interfacial nodes are used to identify whether the materials pull apart from each other, based on which contact conditions are applied as described below:

If $T_{n_{interfacial\ node}} < 0$ (compressive stress state) then the material-material conditions are applied to both colliding nodes (e.g. $A1$ and $A2$).

If $T_{n_{interfacial\ node}} > 0$ (tensile stress state) then the material-void conditions are applied to both colliding nodes. Once the material-void conditions come into play, separation between the materials occurs naturally, i.e. no introduction of a void is necessary; the sharp interfaces are evolved and pull apart due to the independent velocities in the individual interacting materials.

5. RESULTS

The performance of the contact algorithm has been tested for different situations involving planar and oblique impact. Three problems where the collision and separation of the materials are involved have been shown in the current work, viz;

1. Planar impact between two deformable bodies which is shown by simulating the flyer plate impact problem.
2. Planar impact between a deformable body and a rigid body which can be seen in the simulation of a Taylor Bar problem.
3. Oblique impact at 10 degree angle of attack between a projectile and a target leading to ricochet of the projectile.

5.1 Flyer Plate Simulation

The numerical simulation of a plate impact experiment has been used in the past to study the phenomenon of spall fracture [32, 41-43]. A complete description along with the experimental results for spall fracture has been given by Antoun et. al.[44]. Plate impact simulation for the study of spall fracture involves the planar impact and separation of the flyer and the target plates and

hence a contact model plays an important role in capturing the wave physics accurately. In this work the flyer plate simulation has been performed without including the spall phenomenon and is therefore realistic only up to the point of incipient spall at the lower surface. The simulation is performed with the proposed contact model for three different cases in order to validate the wave propagation phenomena in the interacting materials in the period prior to and following separation of the impactor from the target. In the first case, the acoustic impedance of the flyer plate is less than that of target plate; in the second case the flyer plate is of higher acoustic impedance and in the third case the acoustic impedance of the flyer and the target plates are the same. The interaction of the shock waves in these three cases has been discussed in the following.

5.1.1. Acoustic Impedance of Flyer Plate is Less Than Target Plate

In this case the acoustic impedance of the flyer plate (Aluminum) is less than the target plate (Copper). The details regarding the plate's geometric configuration, material properties and the flyer plate velocity have been taken to simulate experimental data(experiment B-61)[45]. The plates are cylindrical in shape as shown in figure 5(a); this allows use of the axisymmetric computational geometry as shown in Figure 5(b). The simulation duration is $10 \mu\text{s}$. The dimensions of the plates along with the impact velocity are tabulated in Table 3.

As shown by theoretical analysis of the wave propagation phenomena in flyer plate impact[44], after the impact takes place shock waves of equal magnitude are generated in both plates. The shock wave in the flyer plate travels into the impactor and interacts with its free surface; due to this interaction, reflection of the wave at the free surface of the flyer takes place which gives rise to the formation of a returning rarefaction wave. This rarefaction wave passes through the flyer plate and interacts with the impacted surface which leads to the formation of tensile stress conditions at the impact interface. Due to this tensile state at the impacted interface the separation of flyer from target plate takes place as seen in figure 6(b). The configurations of the plates before and after the simulation are seen in figure 6 which shows that the contact model was able to handle the impact and separation of the materials.

To validate the results obtained from the simulation, the bottom free surface velocity at a point which is 10 mm from the center of the target plate is compared with available experimental results. The plot is shown in figure 7. The peak velocity at the bottom free surface of the target plate matches well with the experimental data. The graph has been plotted till $t = 0.3 \mu\text{s}$ because after this the effect of spall fracture comes into play. Since we are not using a damage model to study spall fracture in this work the free surface velocity profile obtained from the current work deviate from the experimental results after $t = 0.3 \mu\text{s}$. Grid convergence study has been performed using four different grid sizes viz., $\Delta x = 0.2 \text{ mm}$, 0.1 mm , 0.05 mm and 0.03 mm respectively. The bottom free surface velocity for the grid sizes of $\Delta x = 0.1 \text{ mm}$, 0.05 mm and 0.03 mm at a point 10 mm from the center of the plate has been shown in figure 8 along with the experimental results. This shows the convergence of the contact model as the grid is refined. Also, the peak velocity at the bottom free surface has been considered to calculate an error measure for the four different grid sizes. The error measure is defined as

$$\varepsilon = \frac{|V_{coarse} - V_{finest}|}{V_{finest}} \quad (27)$$

where, V_{coarse} is the peak velocity at the bottom free surface for the coarse grid and V_{fine} is the peak velocity of the finest grid with a grid spacing of 0.03 mm in this case. The four different grid sizes of $\Delta x = 0.2 \text{ mm}$, 0.1 mm , 0.05 mm and 0.03 mm have been considered. The error measure plot with different grid sizes has been shown in figure 9. As seen in the figure the error in calculated bottom surface velocity converges with grid refinement with a near second-order convergence behavior.

5.1.2. Acoustic Impedance of the Flyer Plate is Greater Than Target Plate

The contact treatment is tested next for the case where the acoustic impedance of the flyer plate is greater than the target plate. The impact velocity and plate dimensions remain same as the previous case, but now the flyer plate is Copper and the target plate is Aluminum. The stress-velocity diagram [44] shows that in this case the impacting interface maintains a compressive state throughout the impact and hence both plates should remain in contact and no separation of target and flyer plate is expected. The wave physics involved in this situation is different from the previous one and thus the ability of the present algorithm to accurately portray expected physical behavior is demonstrated through this case.

After the impact takes place an initial shock wave of equal magnitude is generated in both target and projectile in order to maintain the stress and velocity continuity at the impacted interface and denoted as shocks S(Cu) and S(Al) in Figure 10(a). As the thickness of the flyer plate is less than the target material, the shock wave in the projectile, i.e. S (Cu), travels upward and interacts with the free boundary of the flyer plate where it is then reflected as a release wave. This release wave returns to the impact surface and interacts with the target again to generate a shock wave in the flyer plate and a rarefaction wave in the Aluminum target plate as shown in the Figure 10(b). The wave reflection at the free surface of the Copper flyer plate and its interaction with the impacted surface leads to the generation of successive rarefaction waves in the target, i.e. R2, R3 etc. shown in Figure 10(c) and 10(d). These rarefaction waves eventually unload the target material to equilibrium. During the course of these interactions the flyer and target never separate, as expected from the physics of the problem[44].

5.1.3. Acoustic Impedance of the Flyer plate is Equal to Target Plate:

Previous studies of attenuation of shock waves in solids have been conducted for flyer plate impact [46, 47] with the use of the same material for the flyer and the target plates. In this situation, first a shock wave is produced in both flyer and target due to the impact which is the same as in the previous two situations. Once the shock wave propagates into the flyer plate and reaches the rear free surface of the flyer, it reflects as a rarefaction wave which propagates towards the target and unloads the flyer plate to zero stress state. Once this rarefaction wave reaches the impacted interface, it passes through the interface completely because both the materials are of equal impedance. Now, the rarefaction wave moves through the shock compressed portion in the

target plate and it eventually overtakes the initial shock front and leads to the attenuation of the shock wave.

In order to capture this wave physics of attenuation of shock waves, numerical simulation has been performed for the impact between Aluminum-Aluminum plates. The dimension and impact velocity is taken from the work by Fowles[48] in order to compare the simulation results. The variation of peak pressure with the target plate location is shown together with the numerical results from [48] in Figure 11. As can be seen in the figure the computed and theoretical values are in good agreement through the wave interaction process.

It is evident from the results above that the shock wave attenuates while traveling in the target plate. The attenuation begins after the wave has travelled a certain distance inside the material. This is in agreement with the expected physics since the attenuation is caused by the rarefaction wave which returns from the free surface of the flyer plate and catches up with the shock wave in the target plate. This case demonstrates that the contact algorithm is able to handle wave interactions at the interfaces accurately.

5.2. Taylor Bar Impact Simulation:

The simulation of Taylor bar impact is performed in order to assess the performance of the proposed contact model in the situation where a deformable body collides with a rigid body. The bar is made of Tungsten heavy alloy and the test configuration and dimension of the bar is shown in Figure 12. The dimension and impact speed of the bar as shown in figure 12 have been taken from the work by Batra and Stevens[13]. The material properties for the Tungsten Heavy alloy is given in Table 1 and 2. The grid spacing of $\Delta x = 0.1 \text{ mm}$ has been used for this problem in both the directions; this grid spacing has been used to yield a grid independent solution for the current simulation.

The Taylor bar impact simulation results in the deformed configuration shown in Figure 13; contours of effective plastic strain are also shown in the figures. It is evident that due to the development of tensile stress conditions and upward velocity at the bottom of the bar along the outer periphery, the ends of the bar lift off the rigid target and curl upward. The bar radius at the foot and maximum equivalent plastic strain at time $10 \mu\text{s}$ and $50 \mu\text{s}$ for present calculation have been compared with the solutions obtained from Batra and Stevens[13] and is shown in Table 4. Also, the contours of effective plastic strain at time $50 \mu\text{s}$ for current simulation and solutions obtained from Batra and Stevens[13] is shown in Figure 14. The numerical results are in good agreement. This shows the capability of the proposed contact model to handle the collision and separation of a deformable body over a rigid surface.

5.3. Oblique Impact between Two Deformable Bodies:

The problem involving an oblique impact of two bodies is important in practical applications. The phenomenon of ricochet of a projectile over the target has been analyzed in the past to simulate the oblique impact problem[33, 49]. When ricochet results in the situation depicted in Figure 15, there is a sustained interaction between the projectile and the target throughout which the projectile is deflected away and separates from the target. Thus, this case is a stringent test of the ability of the current contact scheme to effect contact-separation behavior in

the present sharp interface Eulerian setting. In order to assess the ability of the contact algorithm to handle oblique impact situations and to capture ricochet phenomena, a high strength steel projectile is impacted on a Tungsten heavy alloy (WHA) target. The angle of impact is 10° and the impact velocity is 1000 m/s . The length to width ratio for the projectile is 10.7 as used in previous work [33]. The grid spacing is 0.2 mm for this simulation. The configuration for the simulation is shown in figure 16. The deformation of the projectile at different times is shown in figure 17.

In this case the contact model is able to predict the sliding between the projectile and the target and the lift-off of the projectile from the target. From figure 17 it can be seen that there is only a modest change in the horizontal velocity during the entire process which explains why momentum loss of the projectile in this case is not significant. The vertical velocities developed due to the impact and ricochet interaction are small compared to the horizontal velocity. Also, the angle with which projectile leaves the target surface is found out to be approximately 9° for the present angle of incidence of 10° . Hence, the angle with which projectile impacts the target is almost the same with which it leaves, which shows the capability of the contact model to handle impact, sliding and separation in the case of inclined impact.

6. CONCLUSIONS

An algorithm for the treatment of separation following contact of material interfaces is presented for a well-established sharp-interface Eulerian high speed multi-material solver. The advantage of the model lies in its ease of implementation; in contrast to Lagrangian contact treatments search operations for detecting collisions are simplified by the use of levelsets and no local constraints to prevent interpenetration through penalty-type force application is necessary to separate interfaces. Since the framework is Eulerian difficulties associated with carrying meshes through the material interactions, managing meshes to retain solution accuracy and stability and detecting contact between interacting surfaces are circumvented. The contact conditions are handled by implicitly satisfying the interfacial conditions on the parts of the interacting material interfaces that are in contact using a modified Ghost Fluid Method. Use of a sharp interface treatment obviates the need to develop special treatments for materials that coexist within a grid cell. Such subgrid material pairs are always maintained as distinct entities separated by sharp interfaces. The results obtained from our numerical simulations match well with experimental data where available and with other numerical simulations. Using the contact model, it is demonstrated that the wave physics involved in flyer plate impact cases have been captured accurately for material pairs of various impedances. The contact algorithm is shown to handle contact with rigid solids in the case of a Taylor bar impact. Finally, oblique impact of a projectile on a target at an 10° angle of impact has been studied using the present contact algorithm and its capability for handling sliding and separation has been shown. The study of ricochet of a projectile obliquely impact a target plate is the subject of ongoing work along with the extension of the algorithm in a three-dimensional parallel computing framework.

7. ACKNOWLEDGEMENTS

This work was performed under grants from the AFOSR Computational Mathematics program (Program Manager: Dr. Fariba Fahroo) and from the AFRL-RWPC (Computational Mechanics Branch, Eglin AFB, Program Manager: Dr. Martin Schmidt).

REFERENCES

1. Zukas JA. *High velocity impact dynamics Chapter 5*. Wiley-Interscience, 1990.
2. Baker J, Williams A. Hypervelocity penetration of plate targets by rod and rod-like projectiles. *International journal of impact engineering* 1987; **5**(1-4): 101-110.
3. Ahrens TJ, O'Keefe JD. Impact on the Earth, ocean and atmosphere. *International journal of impact engineering* 1987; **5**(1): 13-32.
4. Roddy DJ, Schuster SH, Rosenblatt M, Grant LB, Hassig PJ. Computer simulations of large asteroid impacts into oceanic and continental sites--preliminary results on atmospheric, cratering and ejecta dynamics. *International journal of impact engineering* 1987; **5**(1-4): 525-541.
5. Benson DJ, Nellis W. Dynamic compaction of copper powder: Computation and experiment. *Applied physics letters* 1994; **65**(4): 418-420.
6. Benson D, Tong W, Ravichandran G. Particle-level modeling of dynamic consolidation of Ti-SiC powders. *Modelling and Simulation in Materials Science and Engineering* 1995; **3**: 771.
7. Walker JD, Anderson Jr CE. *Multi- material velocities for mixed cells*. in *AIP Conference Proceedings*. 1994.
8. Tran LB, UdayKumar. HS. A particle levelset based sharp interface cartesian grid method for impact, penetration, and void collapse. *Journal of Computational Physics*. 2004; **193**(2): 469-510.
9. Anderson CE. An overview of the theory of hydrocodes. *International journal of impact engineering* 1987; **5**(1): 33-59.
10. Taylor L, Flanagan D, *PRONTO 2D: A two-dimensional transient solid dynamics program*, 1987, Sandia National Labs., Albuquerque, NM (USA).
11. Camacho.G.T., M.Ortiz. Adaptive lagrangian modelling of ballistic penetration of metallic targets. *Comput. Methods Appl. Mech. Eng.* 1997; **142**(3-4): 269-301.
12. Hallquist J, *User's manual for DYNA2D: an explicit two-dimensional hydrodynamic finite element code with interactive rezoning*, 1980, Lawrence Livermore National Lab., CA (USA).
13. Batra R, Stevens J. Adiabatic shear bands in axisymmetric impact and penetration problems. *Computer methods in applied mechanics and engineering* 1998; **151**(3): 325-342.
14. Li S, Qian D, Kam Liu W, Belytschko T. A meshfree contact-detection algorithm. *Computer methods in applied mechanics and engineering* 2001; **190**(24): 3271-3292.
15. Benson DJ. A mixture theory for contact in multi-material Eulerian formulations. *Computer methods in applied mechanics and engineering* 1997; **140**(1): 59-86.
16. Benson DJ, Okazawa S. Contact in a multi-material Eulerian finite element formulation. *Computer methods in applied mechanics and engineering* 2004; **193**(39): 4277-4298.
17. Vitali E, Benson DJ. An extended finite element formulation for contact in multi-material arbitrary Lagrangian-Eulerian calculations. *International journal for numerical methods in engineering* 2006; **67**(10): 1420-1444.
18. Vitali E, *An extended finite element formulation for contact in multi-material arbitrary Lagrangian-Eulerian calculations*, 2007, UC San Diego Electronic Theses and Dissertations: UC San Diego.
19. Vitali E, Benson DJ. Contact with friction in multi- material arbitrary Lagrangian- Eulerian formulations using X-FEM. *International journal for numerical methods in engineering* 2008; **76**(6): 893-921.
20. Vitali E, Lomov I, Antoun T, Fujino D. An extended Eulerian method for contacts in Godunov formulations. *International journal for numerical methods in engineering* 2012.
21. Sethian JA. *Level set methods and fast marching methods: evolving interfaces in computational geometry, fluid mechanics, computer vision, and materials science*. Cambridge Univ Pr, 1999.
22. Sethian J. Evolution, implementation, and application of level set and fast marching methods for advancing fronts. *Journal of Computational Physics* 2001; **169**(2): 503-555.
23. Merriman T, Fedkiw R, Aslam P, Osher S. 'A Non-Oscillatory Eulerian Approach to Interfaces in Multi-Material Flows. *J. Comput. Phys.*, to appear 2003.

24. Sambasivan S,Udaykumar. HS. Ghost Fluid Method for Strong Shock Interactions Part 1: Fluid-Fluid Interfaces. *AIAA*. 2009; **47**(12): 2907-2923.
25. Sambasivan S,Udaykumar. HS. Ghost fluid method for Strong Shock Interactions. Part2: Immersed Solid Boundaries. *AIAA*. 2009; **47**(10): 2923-2937.
26. Sambasivan S, Kapahi A, Udaykumar H. Simulation of high speed impact, penetration and fragmentation problems on locally refined Cartesian grids. *Journal of Computational Physics* 2012.
27. Kapahi A, Sambasivan S, Udaykumar H. Simulation of Collapse and Fragmentation Phenomena in a Sharp Interface Eulerian Setting. *Computers & Fluids* 2012.
28. Kapahi A, Sambasivan S, Udaykumar H. A Three-Dimensional Sharp Interface Cartesian Grid Method for Solving High Speed Multi-Material Impact, Penetration and Fragmentation Problems. *Journal of Computational Physics* 2013.
29. Kapahi A, J.Mousel, S.Sambasivan and H.S.Udaykumar, *Three dimensional compressible multi-material flow computations using a parallelized levelset-based solver.*, in *Plasticity of Crystalline Materials: From Dislocations to Continuum* John Wiley & Sons, 2011.
30. Kapahi A,Udaykumar H. Dynamics of void collapse in shocked energetic materials: physics of void-void interactions. *Shock Waves* 2013: 1-22.
31. Kapahi A, Mousel J, Sambasivan S, Udaykumar H. Parallel, sharp interface Eulerian approach to high-speed multi-material flows. *Computers & Fluids* 2012.
32. Curran D, Seaman L, Shockey D. Dynamic failure of solids. *Physics reports* 1987; **147**(5-6): 253-388.
33. Lee W, Lee HJ, Shin H. Ricochet of a tungsten heavy alloy long-rod projectile from deformable steel plates. *Journal of Physics D: Applied Physics* 2002; **35**: 2676.
34. Plohr BJ,Sharp DH. A conservative Eulerian formulation of the equations for elastic flow. *Advances in Applied Mathematics* 1988; **9**(4): 481-499.
35. Plohr BJ,Sharp DH. A conservative formulation for plasticity. *Advances in Applied Mathematics* 1992; **13**(4): 462-493.
36. Sambasivan SK, *A sharp interface Cartesian grid hydrocode*, 2010: University of Iowa.
37. Simo J,Hughes T. General return mapping algorithms for rate-independent plasticity. *Constitutive laws for engineering materials: theory and applications* 1987; **1**: 221-232.
38. Johnson GR,Cook WH. Fracture characteristics of three metals subjected to various strains, strain rates, temperatures and pressures. *Engineering Fracture Mechanics* 1985; **21**(1): 31-48.
39. Shu CW,Osher S. Efficient implementation of essentially non-oscillatory shock-capturing schemes, II. *Journal of Computational Physics* 1989; **83**(1): 32-78.
40. Dalrymple RA. Particle Methods and Waves, with Emphasis on SPH. 2007.
41. Eftis J, Nemes J, Randles P. Viscoplastic analysis of plate-impact spallation. *International journal of plasticity* 1991; **7**(1): 15-39.
42. Eftis J,Nemes J. Evolution equation for the void volume growth rate in a viscoplastic-damage constitutive model. *International journal of plasticity* 1991; **7**(4): 275-293.
43. Chen Q, Wang J, Liu K. Improved CE/SE scheme with particle level set method for numerical simulation of spall fracture due to high-velocity impact. *Journal of Computational Physics* 2010; **229**(19): 7503-7519.
44. Antoun T, Seaman L, Curran DR, Kanel GI, Razorenov SV, Utkin AV, *Spall fracture*, Springer Verlag: New York, 2003, pp. 49-54.
45. Seaman L, Curran DR, Antoun TH, *Dynamic Failure of Materials. Volume 2-Compilation of Russian Spall Data*, 1998, SRI INTERNATIONAL MENLO PARK CA.
46. Curran DR. Nonhydrodynamic attenuation of shock waves in aluminum. *Journal of Applied Physics* 1963; **34**(9): 2677-2685.
47. Erkman J,Christensen A. Attenuation of shock waves in aluminum. *Journal of Applied Physics* 1967; **38**(13): 5395-5403.

48. Fowles G. Attenuation of the shock wave produced in a solid by a flying plate. *Journal of Applied Physics* 1960; **31**(4): 655-661.
49. Johnson W, Sengupta A, Ghosh S. High velocity oblique impact and ricochet mainly of long rod projectiles: an overview. *International Journal of Mechanical Sciences* 1982; **24**(7): 425-436.

Material	Y_0 (GPa)	B (GPa)	N	C	m	G (GPa)	T_m (K)
Copper [8]	0.4	0.177	1.0	0.025	1.09	43.33	1358
Tungsten [8]	1.51	0.177	0.12	0.016	1.0	124.0	1777
High strength steel[8]	1.50	0.569	0.22	0.003	1.17	77.3	1723
Aluminum[11]	0.324	0.114	0.42	0.002	1.34	26.0	925.0

Table 1: Johnson Cook strength model parameters with reference to Eq (6) where $A = Y_0$ and $\dot{\epsilon}_0^p = 1.0s^{-1}$

Material	ρ_0 (Kg/m ³)	ν	c (W / m - K)	K (J / Kg - K)	Γ_0	c_0 (m / s)	s
Copper	8930	0.35	383.5	401	2.0	3940	1.49
Tungsten heavy alloy	17600	0.29	477	38	1.43	4030	1.24
High strength steel	7850	0.30	134	75	1.16	4570	1.49
Aluminum	2700	0.30	896	166.9	1.99	5386	1.339

Table 2: Parameters for the Mie-Grüneisen E.O.S. for the used materials in simulation

Plate	Material	Diameter (mm)	Thickness (mm)	Impact Velocity (m/s)
Flyer plate	Aluminum	120	$t_1 = 2$	450
Target plate	Copper	120	$t_2 = 15$	-

Table 3: Material, dimensions and impact velocity of the flyer and target plates

Time		Current Simulation	Batra and Stevens[13]
$t = 10 \mu s$	Taylor Bar Deformed Radius (mm)	6.2	6.1
	Maximum Equivalent Plastic Strain	0.50	0.49
$t = 50 \mu s$	Taylor Bar Deformed Radius (mm)	8.3	8.1
	Maximum Equivalent Plastic Strain	2.27	2.20

Table 4: Comparison of deformed bar radius and maximum equivalent plastic strain at time $10 \mu s$ and $50 \mu s$

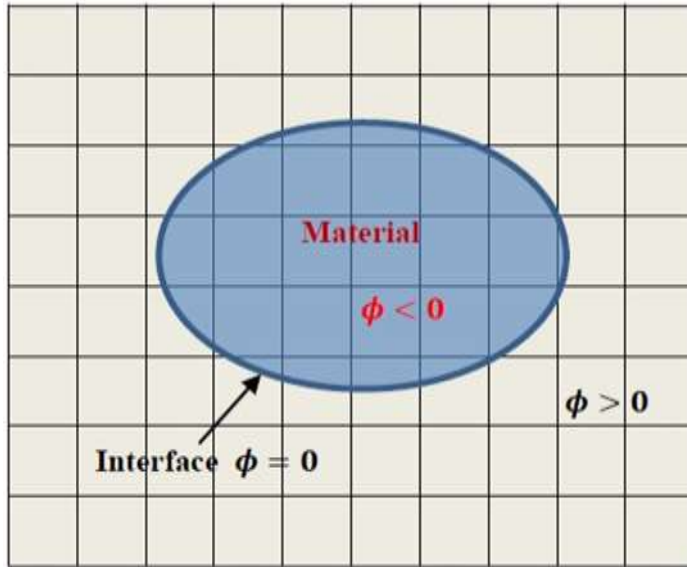


Figure 1: Level Set representation of embedded object

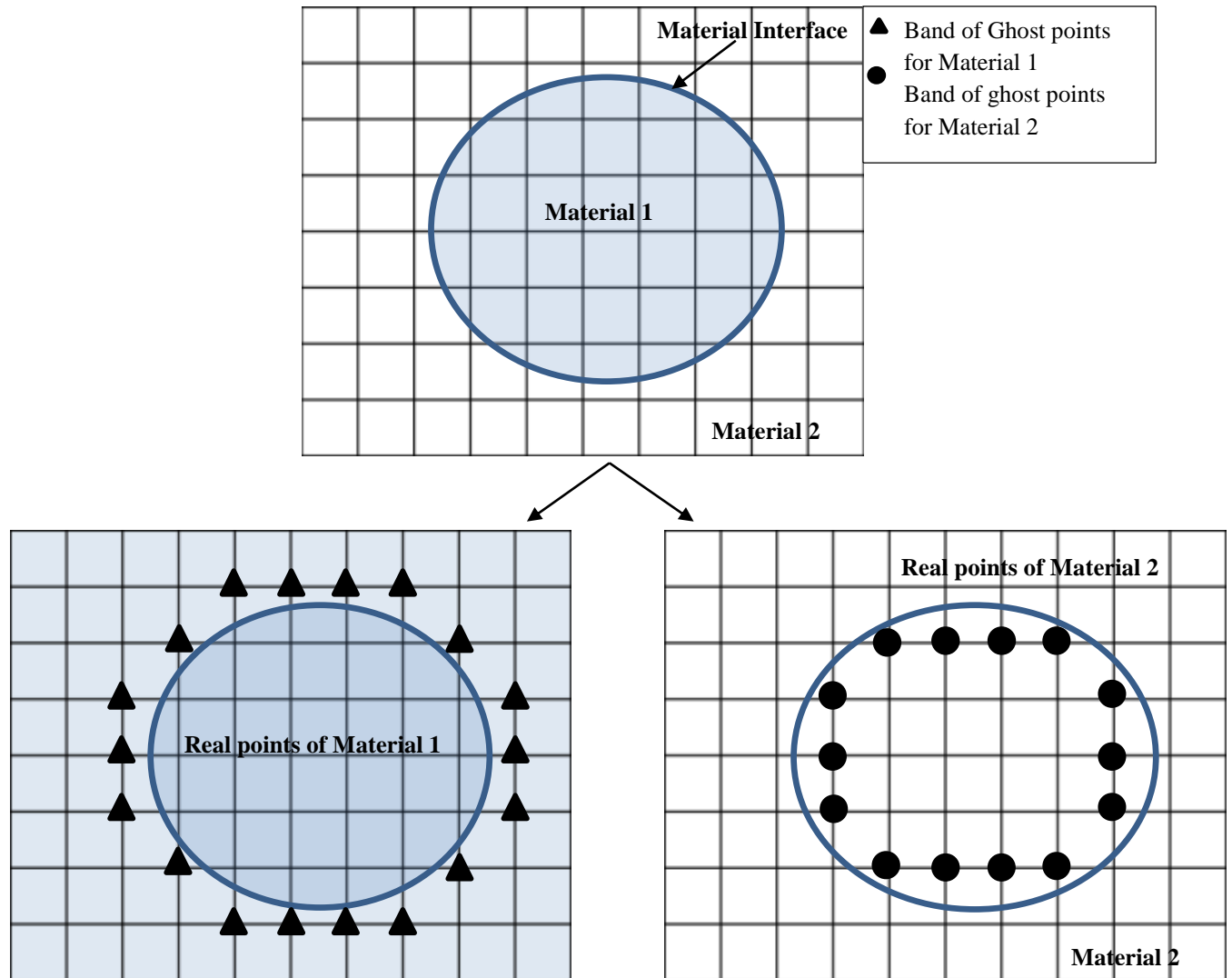


Figure 2: Ghost Fluid Method (GFM) converts a single multi material interaction problem into two single material problems where both materials are treated independently based on their real field and corresponding ghost field

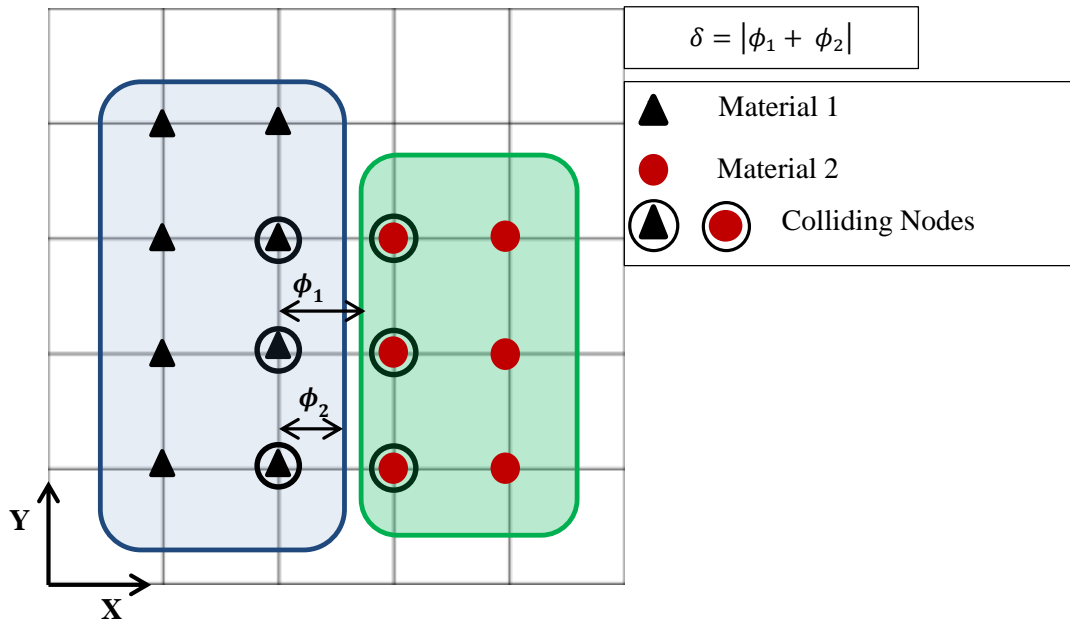
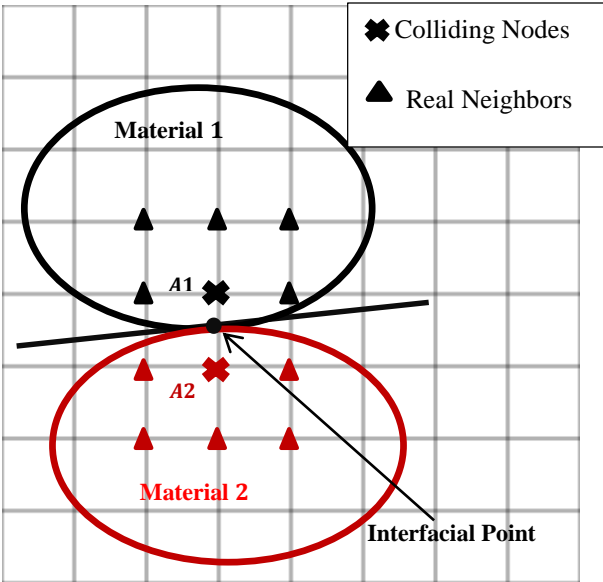
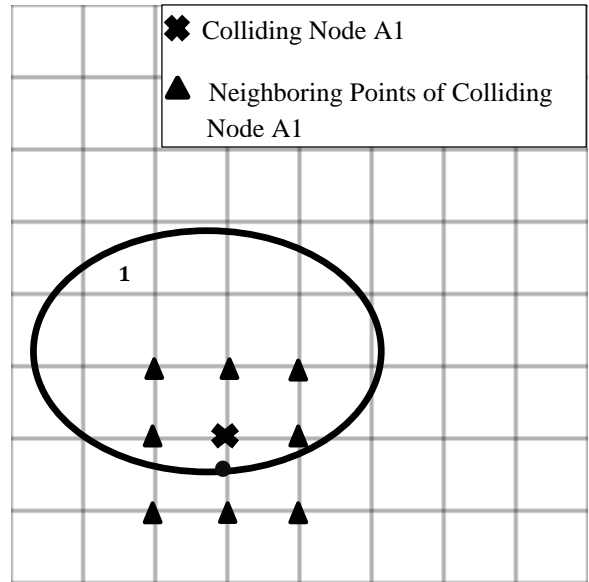


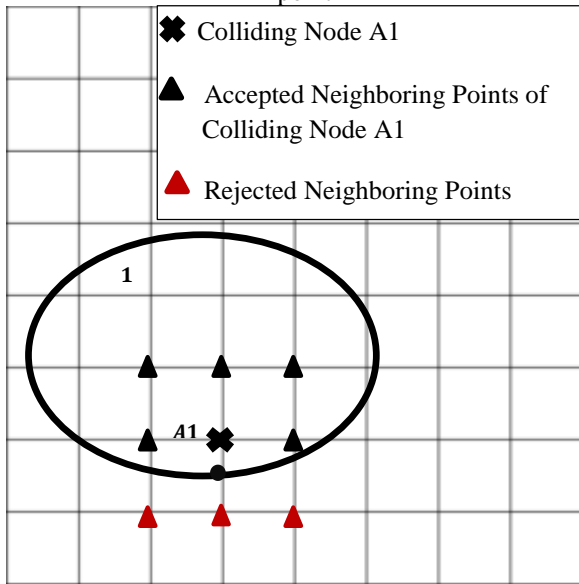
Figure 3: Collision detection procedure between two materials by calculating the relative distance δ between two materials using the level set function ϕ_1 and ϕ_2



(a) Calculation of normal traction at the interfacial point



(b) Neighboring points of the colliding node A1



(c) Accepted points for the construction of least-square field for normal traction

Figure 4: Procedure for the calculation of normal traction at the impacted interfaces between two materials using the least squares method

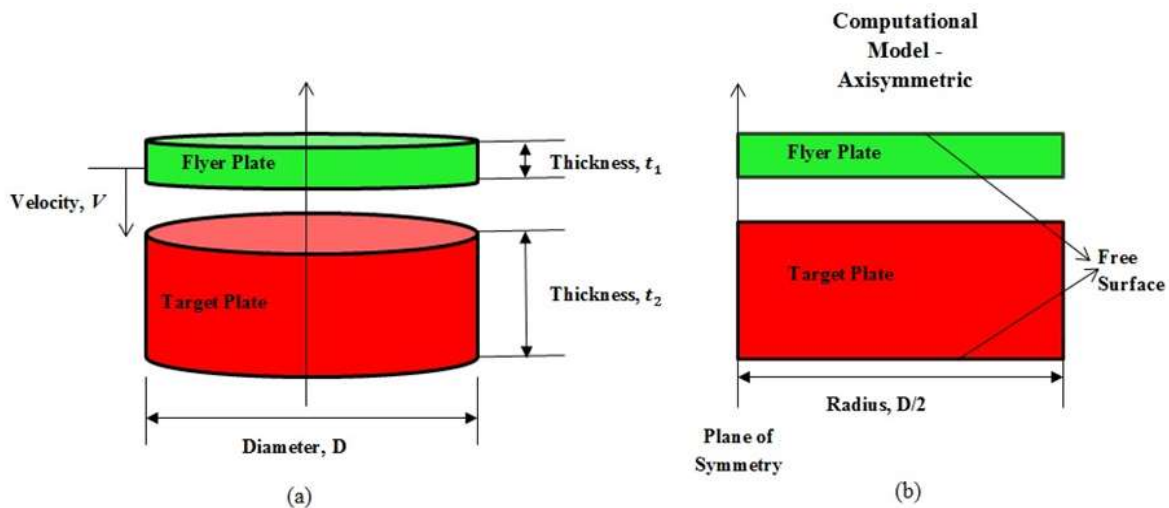


Figure 5: (a) Geometrical sketch of the plate impact experiment, (b) Computational geometry over which simulation is performed.

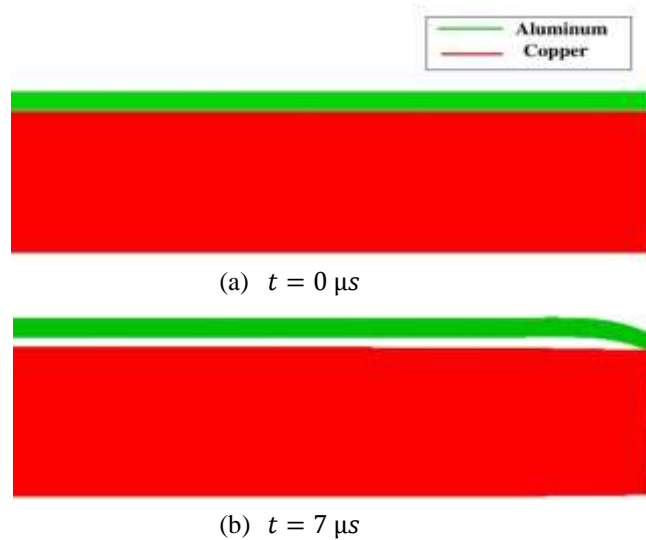


Figure 6: Separation of flyer and target plates after the impact due to the development of tensile stress state at the impacted interface

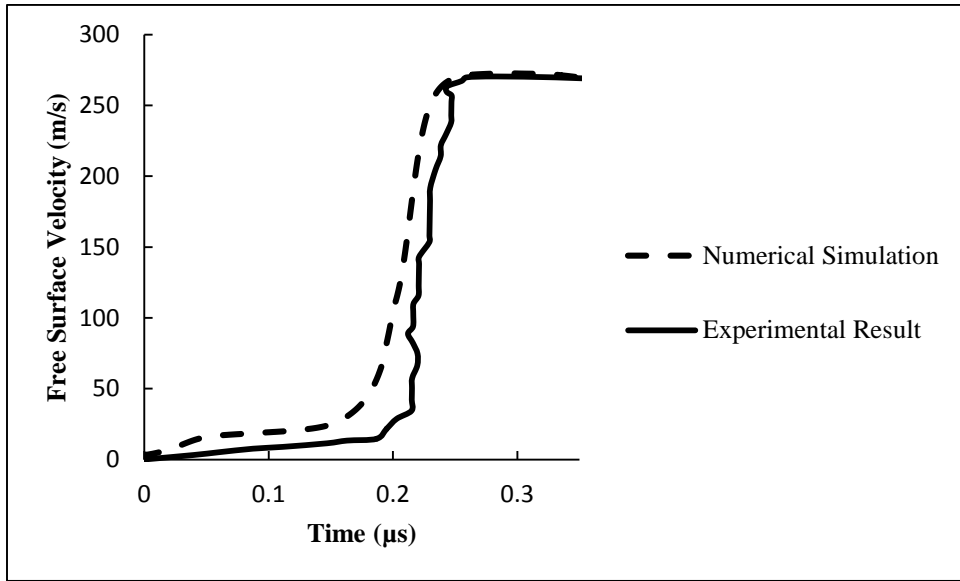


Figure 7: Free surface velocity plots of the target plate vs. time from numerical simulation and experimental results

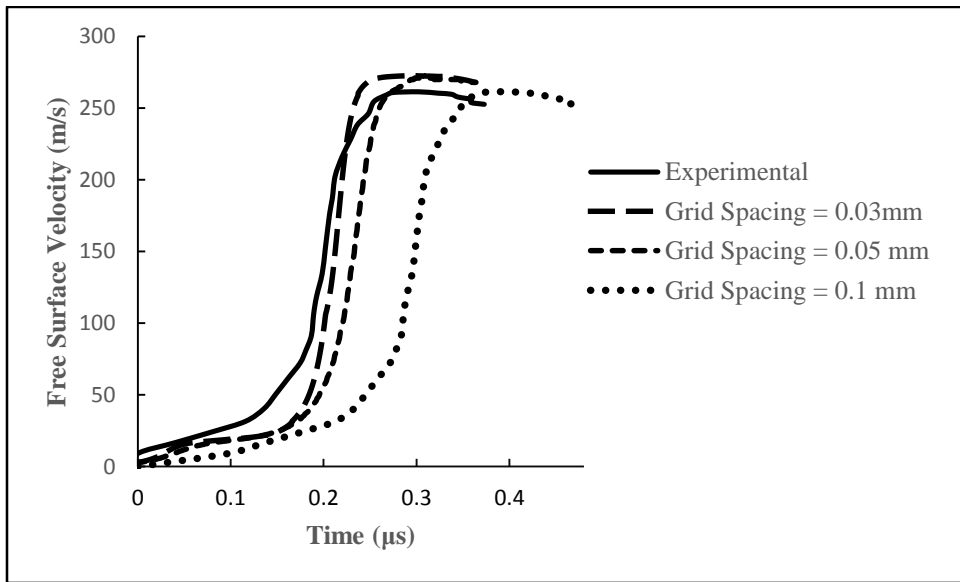


Figure 8: Free surface velocity plots of the target plate vs. time from numerical simulation for three different grid sizes of 0.1 mm, 0.05 mm and 0.03 mm along with the experimental results

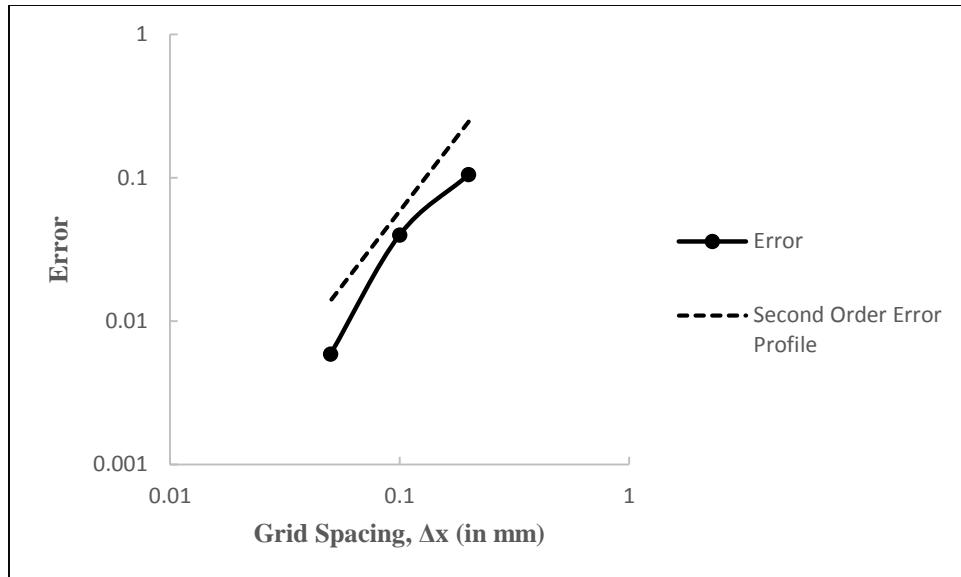
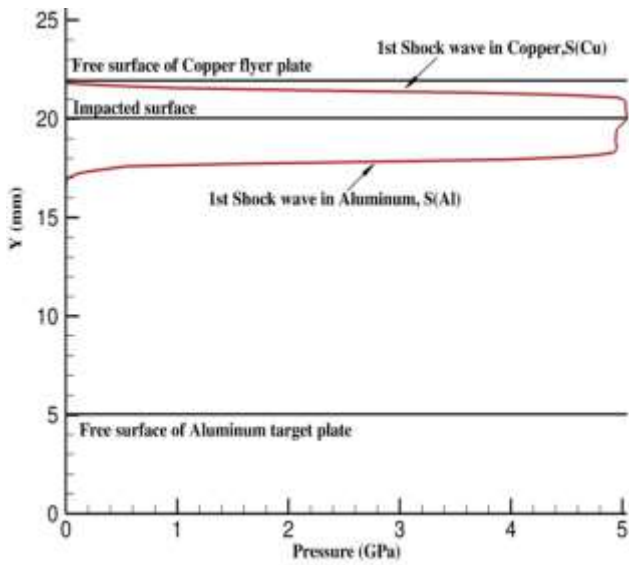
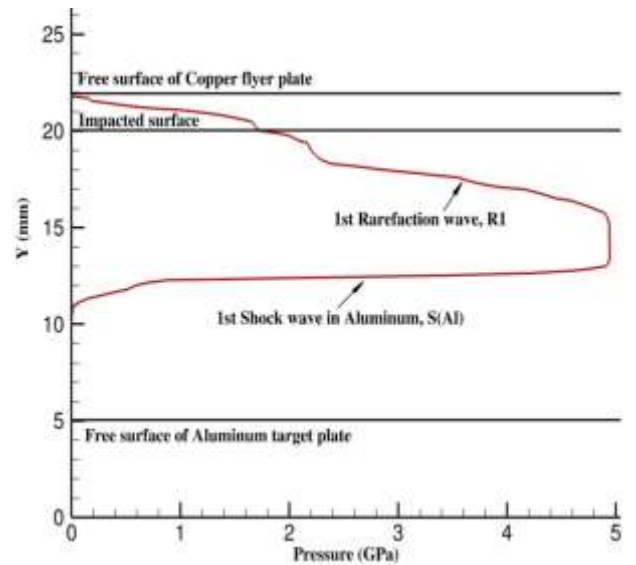


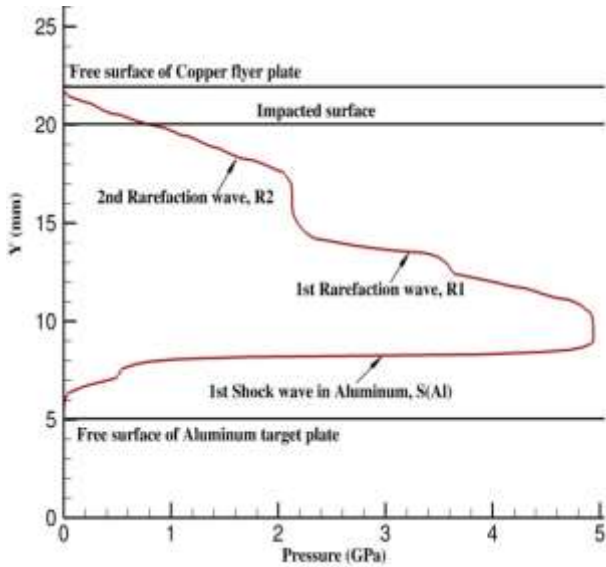
Figure 9: Error measure plot of the peak bottom surface velocity of the target plate with four different grid sizes of 0.2 mm, 0.1 mm, 0.05 mm and 0.03 mm with the second order error estimate plot



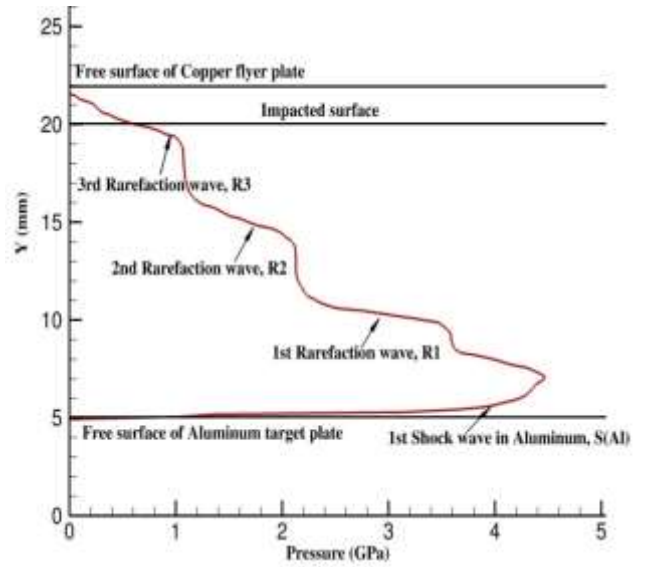
(a) Impact between Copper flyer plate and Aluminum target plate produces shock wave $S(Cu)$ and $S(Al)$ at $t = 0.5 \mu s$ inside both plates



(b) Shock wave $S(Cu)$ after reflection from its top free surface interacts at the impacted surface and produces the first rarefaction $R1$ in the Aluminum plate at $t = 1.5 \mu s$



(c) The impacted surface maintains a compressive stress state which leads to the successive generation of second rarefaction wave $R2$ inside the Aluminum plate at $t = 2.5 \mu s$



(d) The interaction of the wave in the Copper flyer plate with its free surface and the impacted surface produces successive rarefaction wave $R3$ which unloads the Aluminum target plate at $t = 3.5 \mu s$

Figure 10: Wave interaction inside the target plate when impacted by a hard impactor plate at a speed of $450 m/s$, shows gradual decrease in the magnitude of pressure wave while travelling inside the target plate after the impact which leads to unloading of the target plate

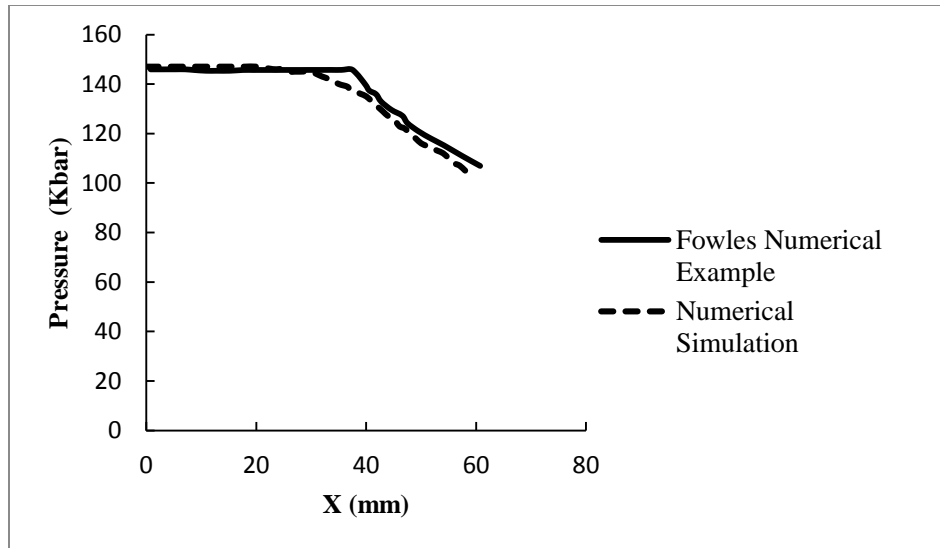


Figure 11: Variation of peak pressure at the shock front as a function of the distance travelled by the shock wave in the target plate

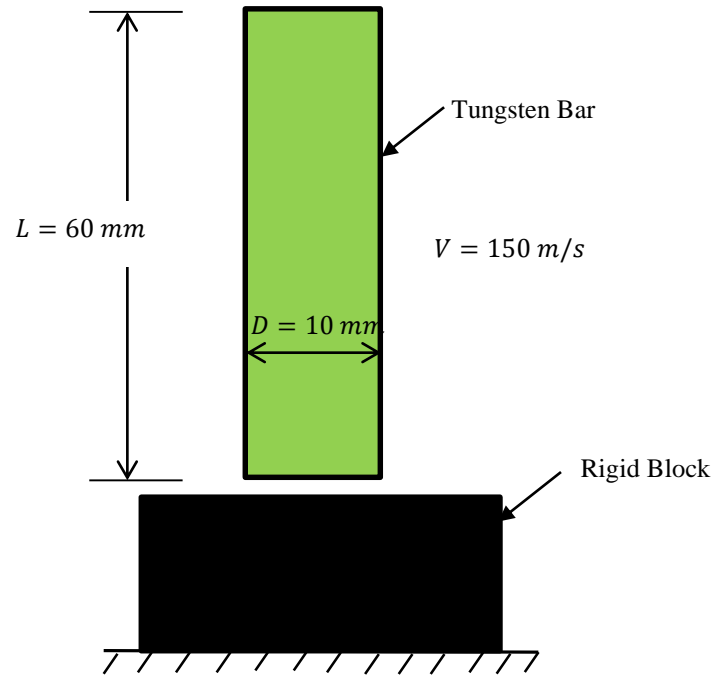


Figure 12: Initial configuration for the simulation of Taylor bar impact problem on a rigid block with a speed of 150 m/s

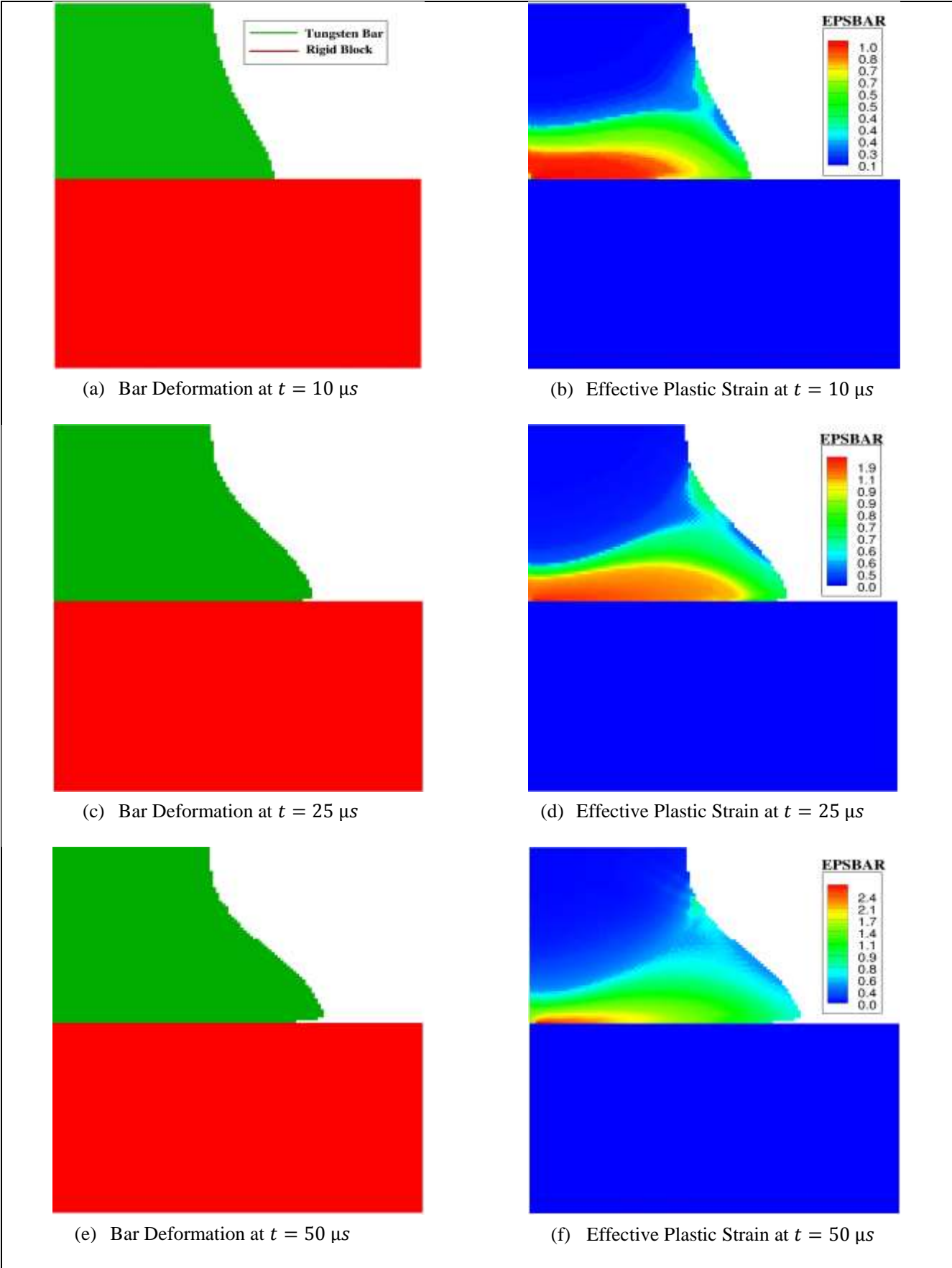
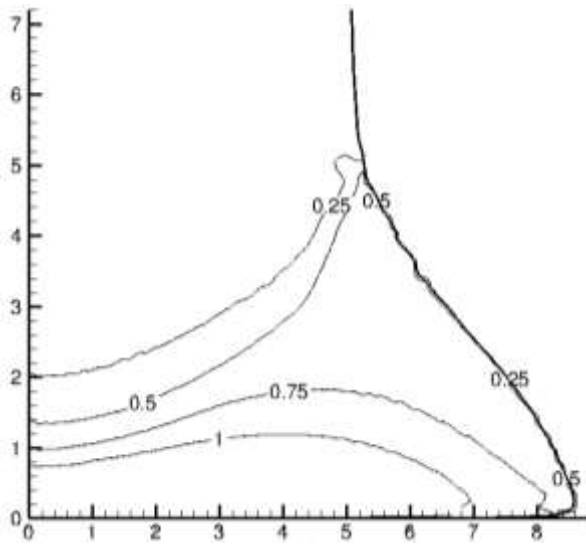
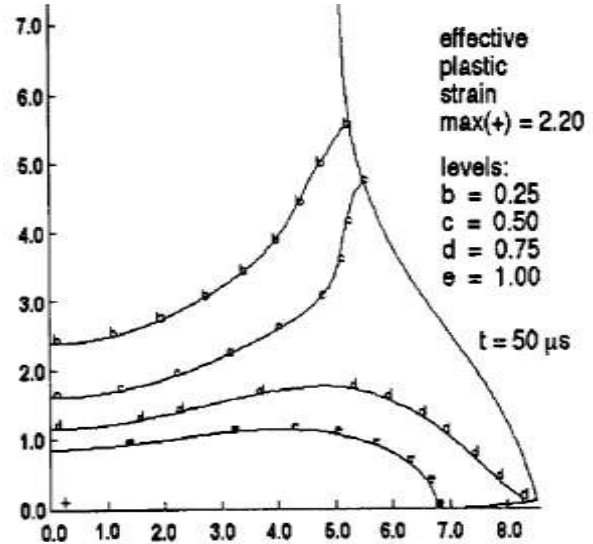


Figure 13: Taylor bar deformation profile and effective plastic strain at different time intervals for the axisymmetric impact of Tungsten bar on a rigid block at a speed of 150 m/s



(a) Current Simulation



(b) Batra and Stevens[13]

Figure 14: Comparison plot of contours of effective plastic strain at $t = 50 \mu s$ with the work of Batra and Stevens[13]

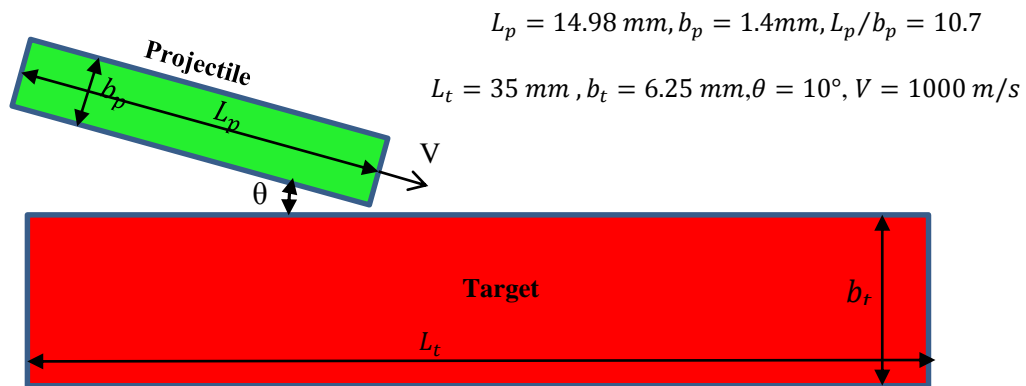


Figure 15: Configuration for the simulation of oblique impact of projectile over the target at 10° angle of attack

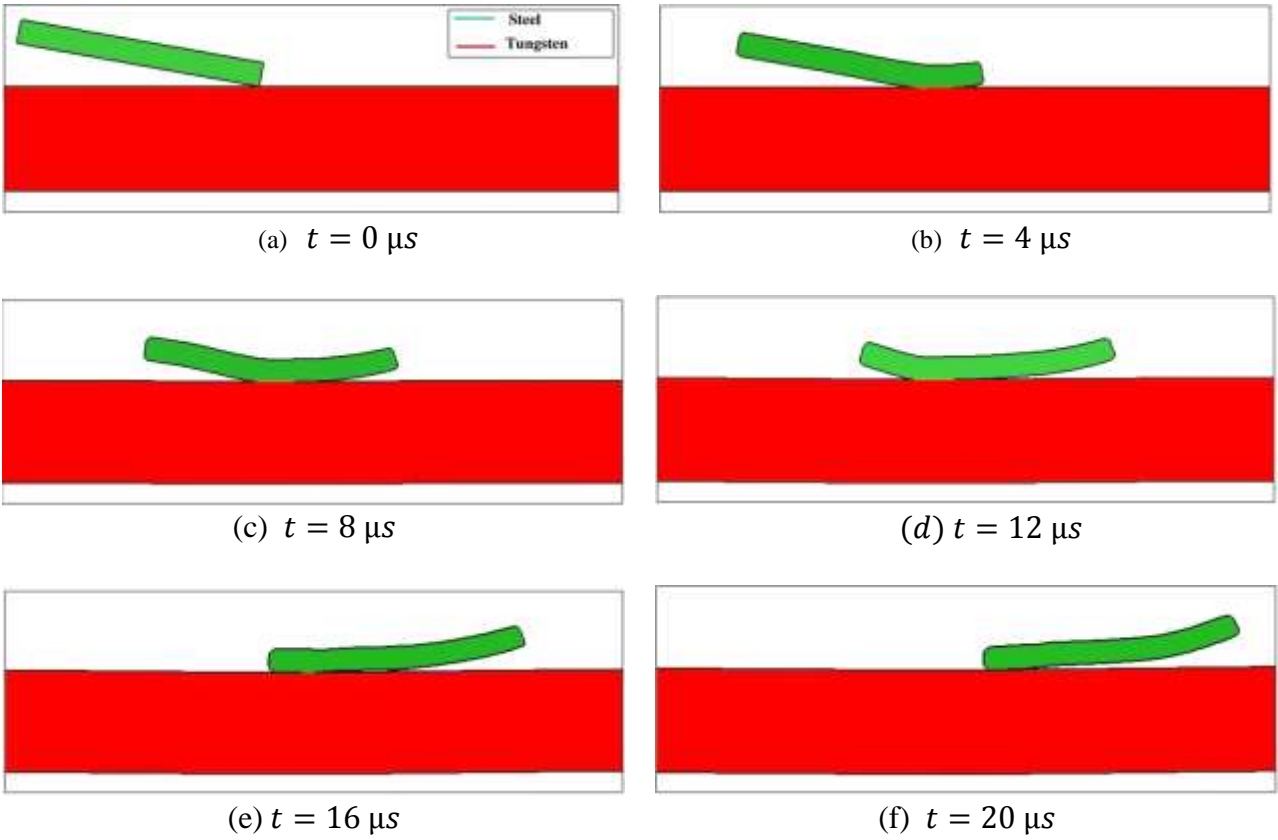


Figure 16: Ricochet of high strength steel projectile over a tungsten target at 10° angle of attack with a speed of 1000 m/s

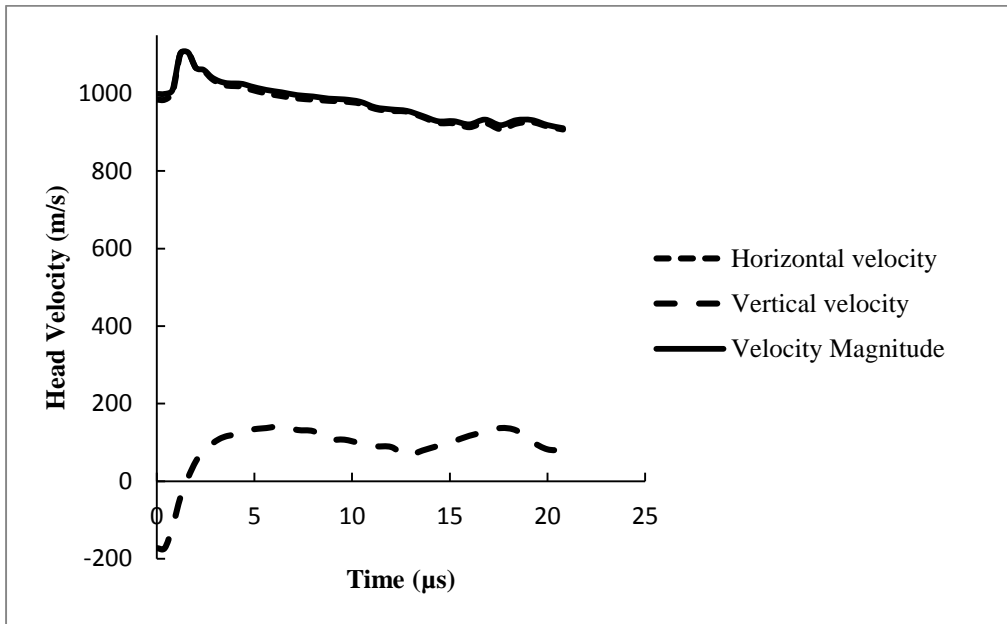


Figure 17: Variation of steel projectile head velocity with time of high strength steel projectile